International Journal of Thermal Sciences 58 (2012) 9–19

Contents lists available at SciVerse ScienceDirect

International Journal of Thermal Sciences

journal homepage: www.elsevier.com/locate/ijts

Slip flow fluid-structure-interaction

J. van Rij, T. Harman, T. Ameel*

Department of Mechanical Engineering, University of Utah, Salt Lake City, UT 84112, USA

ARTICLE INFO

Article history:
Received 8 April 2011
Received in revised form
29 February 2012
Accepted 2 March 2012
Available online 19 April 2012

Keywords:
Microscale
Rarefied flow
Fluid-structure-interaction

ABSTRACT

While many microscale systems are subject to both rarefaction and fluid-structure-interaction (FSI) effects, most commercial algorithms cannot model both, if either, of these for general applications. This study modifies the momentum and thermal energy exchange models of an existing, continuum based, multifield, compressible, unsteady, Eulerian-Lagrangian FSI algorithm, such that the equivalent of first-order slip velocity and temperature jump boundary conditions are achieved at fluid-solid surfaces, which may move with time. Following the development and implementation of the slip flow momentum and energy exchange models, several basic configurations are considered and compared to established data to verify the resulting algorithm's capabilities.

1. Introduction

Both rarefaction and fluid-structure-interaction (FSI) effects are significant for many microscale systems. Examples include micro valves, pumps, actuators, particulate flows, porous flows, two-phase flows, micro-air-vehicles, combustion, and heat exchangers. Rarefaction, typically quantified by the Knudsen number, Kn, which is the ratio of the fluid's mean free path to the characteristic length of the system, becomes significant for gaseous systems at the microscale. Rarefaction results in discontinuities of the velocity and temperature at fluid-solid boundaries, which, for the slip flow regime, $0.01 \leq Kn \leq 0.1$, are typically modeled with first-order slip velocity [1] and temperature jump [2] boundary conditions applied to the continuum based conservation of momentum and energy equations, respectively. FSI effects are significant for any system in which the thermal-fluid and structural dynamics are coupled, and consequently cannot be considered independently. As listed previously, there are already many microsystems that operate with FSI effects; and, as many microfabrication technologies evolve toward the use of more flexible materials than those historically used in the microelectronics industry, such as with printing and molding [3,4], FSI effects may become an even more significant microsystem design consideration. However, while there are many microscale systems that are subject to both rarefaction and FSI effects, currently available computational algorithms do not, typically, have the ability or versatility required to accurately model these effects for a generic microsystem, and as a result, there are few studies which have considered FSI for microsystems [5–20], and no widely available studies that have numerically considered both FSI and rarefaction in a microsystem.

The primary objective of this study is to modify the momentum and energy exchange models of an existing FSI algorithm, such that the equivalent of first-order slip velocity and temperature jump boundary conditions are achieved at fluid-solid boundaries, which may move and deform arbitrarily with time. The FSI algorithm that is utilized is a three-dimensional, unsteady, continuum based Eulerian-Lagrangian methodology in which fluids, modeled using ICE (implicit, continuous fluid, Eulerian) and solid materials, modeled with MPM (the material-point-method), may be modeled either independently or simultaneously. ICE is a finite volume, cell-centered, multimaterial, compressible, computational fluid dynamics (CFD) algorithm that originated at Los Alamos National Laboratory [21,22]. And, MPM is a particle based method for solid mechanics simulations [23,24]. The development and documentation of the MPM-ICE implementation currently utilized is given in [25–28]. The MPM-ICE FSI algorithm utilizes a statistically averaged, or 'multifield,' approach, where, each material is continuously defined (ρ, $\boldsymbol{u}$, e, T, v, θ, $\boldsymbol{\sigma}$, P), with some probability, over the entire computational domain. This approach differs from the perhaps more common, separate domain methodology, in which fluid and solid materials are defined separately, with only one material at each point, and interaction only occurring at material boundaries. The multifield approach is advantageous for the current application, because it tightly couples fluid-structure-interactions through the conservation equations, rather than explicitly though specified boundary conditions, which allows arbitrary distortion of material

* Corresponding author. Tel.: +1 801 585 9730; fax: +1 801 585 9826.
E-mail address: ameel@mech.utah.edu (T. Ameel).

1290-0729/$ – see front matter © 2012 Elsevier Masson SAS. All rights reserved.
doi:10.1016/j.ijthermalsci.2012.03.001

Nomenclature

A	cell fluid-solid surface area
A_c	fin cross sectional area
Bi_D	Biot number, hD/k_s
C	Stokes drag coefficient, $C_D\mathrm{Re}/2$
c	speed-of-sound
C_D	drag coefficient, $F_D/(1/2)\rho_\infty u_\infty^2 DL$
cfl	Courant–Friedrichs–Lewy number
c_p	specific heat at constant pressure
c_v	specific heat at constant volume
D	diameter or characteristic length
e	internal energy per unit mass
E	Young's modulus of elasticity, $9GK/(G+3K)$
$\boldsymbol{f}$	force per unit volume
F_D	drag force
Fo	Fourier number, $\alpha t/D^2$
G	shear modulus of elasticity
H_{rs}	thermal energy exchange coefficient
H_{rs}^{slip}	slip flow thermal energy exchange coefficient
h	heat transfer coefficient or channel height
I	moment of inertia
K	bulk modulus of elasticity
K_{rs}	momentum exchange coefficient
K_{rs}^{slip}	slip flow momentum exchange coefficient
k	thermal conductivity
Kn	Knudsen number, λ/D
L	length
L_2	norm, $\|x\|_2 = \sqrt{\sum_{i=1}^n x_i^2}$
Ma	Mach number, $\mathrm{Re}Kn\sqrt{2/(\pi\gamma)}$
N	number of materials
Nu	Nusselt number, hD/k
P	pressure
p	order-of-accuracy, $\log((\Phi_{2\Delta x}-\Phi_{4\Delta x})/(\Phi_{\Delta x}-\Phi_{2\Delta x}))/\log(2)$
Pr	Prandtl number, $c_p\mu/k$
Q	rotation matrix
q	thermal energy exchange rate per unit volume
q''	heat flux
R	gas constant
Re	Reynolds number, $\rho uD/\mu$
RMS	root-mean-square, $x_{\mathrm{rms}} = \sqrt{(1/n)\sum_{i=1}^n x_i^2}$
T	temperature
t	time
T_b	fin base temperature
$\boldsymbol{u}$	velocity vector
V	cell volume
$\boldsymbol{x}$, $\boldsymbol{y}$, $\boldsymbol{z}$	Cartesian coordinate directions
$\boldsymbol{x'}$, $\boldsymbol{y'}$, $\boldsymbol{z'}$	surface coordinate directions

Greek symbols

α	thermal diffusivity, $k/\rho c_p$
β_t	first-order temperature jump coefficient, $[(2-\sigma_t)/\sigma_t][2\gamma/(1+\gamma)][k/(c_p\mu)]$
β_v	first-order velocity slip coefficient, $(2-\sigma_v)/\sigma_v$
γ	ratio of specific heats, c_p/c_v
δ	fin deflection
θ	volume fraction
Θ	nondimensional temperature, $(T-T_\infty)/(T_b-T_\infty)$
λ	mean free path, $\mu/\rho\sqrt{2RT/\pi}$
μ	dynamic viscosity
ν	kinematic viscosity, μ/ρ
ρ	density
$\boldsymbol{\sigma}$	stress
σ_t	thermal accommodation coefficient
σ_v	momentum accommodation coefficient
$\boldsymbol{\tau}$	shear stress
v	specific volume
ϕ	rotation angle about the $\boldsymbol{z}$-axis
Φ	numerical result
ψ	rotation angle about the $\boldsymbol{y}$-axis

Subscripts

∞	freestream value
i	inlet value
m	mean value
o	outlet value
r	material index
s	material index
w	wall value
x, y, z	Cartesian coordinate directions

Superscripts

-	before exchange contribution
+	after exchange contribution
0	initial value

and material surfaces without explicit surface tracking, passing of boundary conditions, and excessive stability and convergence issues. Use of the MPM-ICE algorithm to evaluate rarefaction with FSI is further merited, as rarefaction effects have already been successfully modeled utilizing the independent CFD (ICE) portion of the algorithm, with slip boundary conditions implemented at the computational domain boundaries [29–31].

The multimaterial governing conservation equations employed by the MPM-ICE algorithm, without effects that are not considered in the present research (chemical reactions, turbulence, multiphase Reynolds stress, gravity, etc.), are given in Eqs. (1)–(3) [28].

$$\frac{\partial \rho_r}{\partial t} + \nabla\cdot(\rho \boldsymbol{u})_r = 0 \tag{1}$$

$$\frac{\partial (\rho \boldsymbol{u})_r}{\partial t} + \nabla\cdot(\rho \boldsymbol{u}\boldsymbol{u})_r = -\theta_r \nabla P + \nabla\cdot(\theta\tau)_r + \sum_{s=1}^N \boldsymbol{f}_{rs} \tag{2}$$

$$\frac{\partial (\rho e)_r}{\partial t} + \nabla\cdot(\rho e \boldsymbol{u})_r = -\frac{P\theta_r}{v_r}\frac{dv_r}{dt} + (\theta\tau)_r : \nabla \boldsymbol{u}_r + \nabla\cdot(\theta k \nabla T)_r + \sum_{s=1}^N q_{rs} \tag{3}$$

Equations (1)–(3) are the ensemble average, r-material, conservation of mass, momentum, and energy equations respectively, where there are N materials, θ_r is the r-material volume fraction, and $\sum_{s=1}^N \boldsymbol{f}_{rs}$ and $\sum_{s=1}^N q_{rs}$ are models for the momentum and energy exchange between materials. Eqs. (1)–(3), along with individual material constitutive or equation-of-state models, and models for $\sum_{s=1}^N \boldsymbol{f}_{rs}$ and $\sum_{s=1}^N q_{rs}$, form a complete system of equations. The detailed numerical solution strategy utilized by the MPM-ICE algorithm to solve this system of equations is presented in [28], and consequently will not be duplicated here. However, in a few words, the numerical approach involves operator splitting. For each timestep, the quantities on the right-hand-side of Eqs. (1)–(3) are computed first - this is the Lagrangian phase of the timestep. The conserved quantities, that is, mass, momentum, and energy, for

fluid materials are accounted for at the cell centers; while, the conserved quantities for solid materials are accounted for at the material particles. Consequently, during the Lagrangian phase, which is executed primarily within the cell-centered ICE framework, the solid materials are dually represented, both, at the particles, and at the cell centers, where the solid material conservation quantities are interpolated. In the second phase of the timestep, the Eulerian phase, the contribution due to advection, that is, the second term on the left of Eqs. (1)–(3), is added to the Lagrangian phase values, where the advected contributions are computed for fluid materials by ICE, and for solid materials by MPM. As such, during the Lagrangian phase, models for both the momentum and energy exchange between materials, $\sum_{s=1}^{N}\boldsymbol{f}_{rs}$ and $\sum_{s=1}^{N}q_{rs}$, respectively, are utilized, while during the Eulerian phase, only the momentum exchange model is utilized to determine the advecting velocity.

The momentum and energy exchange models currently employed by the MPM-ICE algorithm to model FSI for standard continuum conditions ($Kn \approx 0$), are given in Eqs. (4) and (5).

$$\sum_{s=1}^{N}\boldsymbol{f}_{rs} = \sum_{s=1}^{N}K_{rs}\theta_r\theta_s(\boldsymbol{u}_s - \boldsymbol{u}_r) \tag{4}$$

$$\sum_{s=1}^{N}q_{rs} = \sum_{s=1}^{N}H_{rs}\theta_r\theta_s(T_s - T_r) \tag{5}$$

Eq. (4) models $\boldsymbol{f_{rs}}$, the force per unit volume on material r, due to interaction with material s, as a function of the scalar momentum exchange coefficient, K_{rs}, the material volume fractions, and the relative velocity between the two materials. Similarly, Eq. (5) models q_{rs}, the thermal energy exchange rate per unit volume for material r, due to interaction with material s, as a function of the scalar energy exchange coefficient, H_{rs}, the material volume fractions, and the temperature difference between the two materials. To avoid stability and convergence restrictions, the momentum and thermal energy exchange between materials is calculated within each cell implicitly, for each timestep, as shown in Eqs. (6) and (7).

$$\rho_r\boldsymbol{u}_r^{+} = \rho_r\boldsymbol{u}_r^{-} + \Delta t\sum_{s=1}^{N}K_{rs}\theta_r\theta_s(\boldsymbol{u}_s^{+} - \boldsymbol{u}_r^{+}) \tag{6}$$

$$\rho_r c_{v,r}T_r^{+} = \rho_r c_{v,r}T_r^{-} + \Delta t\sum_{s=1}^{N}H_{rs}\theta_r\theta_s\left(T_s^{+} - T_r^{+}\right) \tag{7}$$

The '−' and '+' superscripts in Eqs. (6) and (7) indicate values before and after the momentum and thermal energy exchange between materials, respectively, at the point in the timestep that the exchange contributions are calculated. It is assumed with the calculation of Eqs. (6) and (7) that the material masses, volume fractions, and specific heats are not modified by the momentum and energy exchange between materials. (The exchange of mass, momentum, and energy due to a chemical reaction, although not consider in this study, would be modeled with additional terms in the governing equations, not Eqs. (4) and (5), as discussed in [28].) It is also necessary with the implementation of Eqs. (6) and (7) to specify momentum and energy exchange coefficients for all possible material pairs. However, K_{rs} must equal K_{sr}, and H_{rs} must equal H_{sr}, since the force, and heat transferred, from material r due to material s is equal and opposite the force, and heat transferred, from material s due to material r. And, $K_{rr} = H_{rr} = 0$, because the stress and heat flux within the same material are already accounted for with other terms of the momentum and energy conservation equations. A very large momentum transfer rate between materials r and s, specified by a large K_{rs} value, forces the relative velocity of the two materials to zero, consistent with a no-slip velocity boundary condition. Similarly, a large H_{rs} value produces a large thermal energy transfer rate between materials r and s, resulting in the equivalent of a thermal equilibrium boundary condition. In the current algorithm, K_{rs} and H_{rs} values are typically specified as arbitrarily large, constant, scalar quantities ($\sim 1\times 10^{15}$), which result in momentum and thermal energy transfer rates that are not directional relative to the fluid-solid surface, but produce the intended effect of conventional no-slip velocity and thermal equilibrium boundary conditions.

The objective of this study, as stated previously, is to modify the momentum and energy exchange models of the FSI algorithm described, such that both rarefaction and FSI effects are accurately represented for a generic microsystem operating in the slip flow regime. Following the development and implementation of the slip flow momentum and energy exchange models, several basic configurations are considered and compared to established data to verify the resulting algorithm's capabilities. These verifications include: 1) velocity profiles of a rarefied gas between parallel plates; 2) temperature profiles of a rarefied gas between parallel plates; 3) drag coefficients, C_D, and Nusselt numbers, Nu, for low Reynolds number rarefied flow around an infinite cylinder; and, 4) the transient, thermal/structural response of a damped-oscillatory three-dimensional finite cylinder subject to an impulsively started uniform, rarefied flow.

2. Slip flow modifications

Several modifications to the momentum and energy exchange models in the MPM-ICE FSI algorithm must be implemented to correctly model the momentum and energy exchange between a rarefied gas and a moving, deforming solid surface. First, slip flow momentum and energy exchange coefficients, K_{rs}^{slip} and H_{rs}^{slip}, respectively, must be derived as a function of the level of rarefaction. Then, the slip flow momentum and thermal energy exchange models, with a tensor momentum exchange coefficient, must be applied at fluid-solid surfaces.

2.1. Slip flow momentum and energy exchange coefficients

The tangential momentum exchange between a rarefied gas, denoted as material r, and a solid material, material s, is described by the first-order slip velocity boundary condition, Eq. (8) [1]. To obtain the force per unit volume on the rarefied gas due to interaction with the solid, $\boldsymbol{f_{rs}}$, the shear stress on the gas, $-\tau$ from Eq. (8), is multiplied by the fluid-solid surface area in the cell, A, as well as the gas volume fraction, θ_r, and then divided by the cell volume, V, as shown in Eq. (9). For $\boldsymbol{f}_{rs}$ in Eq. (9) to be equivalent to the momentum exchange model utilized by the algorithm, Eq. (4), the slip flow tangential momentum exchange coefficient, K_{rs}^{slip}, must be that given by Eq. (10).

$$\boldsymbol{u_r} - \boldsymbol{u_s} = \frac{\beta_v\lambda_r}{\mu_r}\boldsymbol{\tau} \tag{8}$$

$$\boldsymbol{f}_{rs} = -\theta_r\boldsymbol{\tau}\left(\frac{A}{V}\right) = \left(\frac{\theta_r\mu_r}{\beta_v\lambda_r}\right)\left(\frac{A}{V}\right)(\boldsymbol{u}_s - \boldsymbol{u}_r) \tag{9}$$

$$K_{rs}^{slip} = \left(\frac{\mu_r}{\beta_v\lambda_r}\right)\left(\frac{A}{V}\right)\left(\frac{1}{\theta_s}\right) \tag{10}$$

In a similar fashion, using the first-order temperature jump boundary condition, Eq. (11) [2], and the energy exchange model, Eq. (5), the slip flow energy exchange coefficient is obtained in Eqs. (12)and(13).

$$T_r - T_s = -\frac{\beta_t\lambda_r}{k_r}q'' \tag{11}$$

$$q_{rs} = \theta_r q''\left(\frac{A}{V}\right) = \left(\frac{\theta_r k_r}{\beta_t\lambda_r}\right)\left(\frac{A}{V}\right)(T_s - T_r) \tag{12}$$

$$H_{\mathrm{rs}}^{\mathrm{slip}} = \left(\frac{k_{\mathrm{r}}}{\beta_{\mathrm{t}}\lambda_{\mathrm{r}}}\right)\left(\frac{A}{V}\right)\left(\frac{1}{\theta_{\mathrm{s}}}\right) \tag{13}$$

$K_{\mathrm{rs}}^{\mathrm{slip}}$, Eq. (10), and $H_{\mathrm{rs}}^{\mathrm{slip}}$, Eq. (13), are functions of the rarefied gas viscosity, μ_r, thermal conductivity, k_r, and mean free path, λ_r; the solid material volume fraction, θ_s; the first-order slip velocity and temperature jump coefficients, β_v and β_t, respectively; and, the computational cell fluid-solid surface area, A, and volume, V. The cell fluid-solid surface area, A, is approximated according to Eq. (14), as suggested in [32], where Δx, Δy, and Δz are the cell dimensions in each coordinate direction, and y'_x, y'_y, and y'_z are components of the solid surface unit density gradient vector, as will be discussed in *2.2*. Eq. (14) is not exact, but results in good estimates globally, as well as locally if the surface is approximately parallel to any of the coordinate directions.

$$A = \frac{\Delta x \Delta y \Delta z}{y'_{\mathrm{x}}\Delta x + y'_{\mathrm{y}}\Delta y + y'_{\mathrm{z}}\Delta z} \tag{14}$$

Values for μ_r, k_r, θ_s, and V are available within the unmodified algorithm, and values for β_v, β_t, and λ_r are calculated according to Eqs. (15)–(17), respectively [1,2].

$$\beta_{\mathrm{v}} = \frac{2-\sigma_{\mathrm{v}}}{\sigma_{\mathrm{v}}} \tag{15}$$

$$\beta_{\mathrm{t}} = \left(\frac{2-\sigma_{\mathrm{t}}}{\sigma_{\mathrm{t}}}\right)\left(\frac{2\gamma_{\mathrm{r}}}{1+\gamma_{\mathrm{r}}}\right)\left(\frac{k_{\mathrm{r}}}{c_{\mathrm{p,r}}\mu_{\mathrm{r}}}\right) \tag{16}$$

$$\lambda_{\mathrm{r}} = \frac{\mu_{\mathrm{r}}}{\rho_{\mathrm{r}}\sqrt{2c_{\upsilon,\mathrm{r}}(\gamma_{\mathrm{r}}-1)T_{\mathrm{r}}/\pi}} \tag{17}$$

The momentum accommodation coefficient, σ_v in Eq. (15), and the thermal accommodation coefficient, σ_t in Eq. (16), must be measured experimentally. Values for σ_v and σ_t range from zero to one, where $\sigma_v = 0$ represents completely specular reflection, $\sigma_v = 1$ represents completely diffuse reflection, and $\sigma_t = 1$ corresponds to a perfect energy exchange. Experimentally measured values for σ_v and σ_t are, however, typically near unity, and consequently, are approximated as such for all calculations presented within this study. For example, with $\sigma_v = \sigma_t = 1$, and using typical properties for air, $\gamma = 1.4$ and $Pr = 0.7$, β_v and β_t would then be 1.0 and 1.667 respectively. The rarefied gas mean free path, λ_r, Eq. (17), is calculated for each cell of the computational domain, at the beginning of each timestep, as a function of μ_r, ρ_r, $c_{v,r}$, γ_r, and T_r. In the following studies, constant values are utilized for μ_r, $c_{v,r}$ and γ_r, while T_r and ρ_r vary spatially and temporally since ICE is compressible flow algorithm. It should also be noted that, thermal creep flow has not been accounted for in this derivation of K_{rs}^{slip}. Thermal creep flow may be significant in the slip flow regime, and consequently, may be considered in subsequent studies; the present study however, will focus on verifying the first-order slip velocity and temperature jump boundary conditions before considering such second-order effects.

2.2. Slip flow momentum and thermal energy exchange between materials

The original slip velocity and temperature jump boundary conditions given in Eqs. (8) and (11) [1,2], were derived with the assumption that a rarefied gas flow within the slip flow regime may be accurately approximated as a continuum everywhere except at the fluid-solid boundaries. To accurately model a flow within the slip flow regime the numerical algorithm must, likewise, produce continuous velocity and temperature fields everywhere except at the fluid-solid boundaries. Because each material is continuously defined in the MPM-ICE algorithm, this means that approximately equivalent temperatures for each material within the same cell must be obtained, and approximately equivalent velocities for each material within the same cell must be obtained everywhere, except at the fluid-solid boundaries where discontinuities in the velocity and temperature between the fluid and solid materials may occur. Therefore, the unmodified K_{rs} and H_{rs}, i.e. the arbitrary large, constant, scalar values that result in negligible velocity and temperature differences between materials within the same cell, are applied in the usual manner everywhere except at the fluid-solid surface. At the fluid-solid surface, slip flow momentum and energy exchange coefficients, $K_{\mathrm{rs}}^{\mathrm{slip}}$ and $H_{\mathrm{rs}}^{\mathrm{slip}}$, respectively, must be applied – once the fluid-solid surface is identified. In the MPM algorithm, solid materials are modeled with material particles, typically eight particles per cell. As such, a surface is identified as a cell that has material particles of the specified solid material, but with less than eight particles. Because the surface may be in motion, and surfaces are not explicitly tracked, it is necessary with this approach to test each cell of the computational domain, with each timestep, to determine if it is a surface cell. If a surface cell is identified, $K_{\mathrm{rs}}^{\mathrm{slip}}$ and $H_{\mathrm{rs}}^{\mathrm{slip}}$, as defined in Eqs. (10) and (13), are then calculated for that cell.

Temperature is a scalar quantity, and consequently, once a surface cell is identified, and $H_{\mathrm{rs}}^{\mathrm{slip}}$ is calculated, calculation of the thermal energy exchange between materials in that cell may precede using the usual algorithm, that is, the numerical implementation of Eq. (7), with $H_{\mathrm{rs}}^{\mathrm{slip}}$ rather than H. Velocity, however, is a vector quantity, and the momentum exchanged between materials must take place with respect to the coordinate system in which the velocity components are defined. In the unmodified algorithm, K_{rs} does not change with direction, and so, the exchange of momentum between materials may be executed in the arbitrary global Cartesian coordinate system, $(\boldsymbol{x},\boldsymbol{y},\boldsymbol{z})$, in which, the velocities are originally defined. However, because $K_{\mathrm{rs}}^{\mathrm{slip}}$ is only applicable in the fluid-solid surface tangential direction, while the standard no-slip K_{rs} must be applied in the fluid-solid surface normal direction, the momentum exchange between materials for slip flow must be executed in a coordinate system defined by the fluid-solid surface. The surface coordinate system $(\boldsymbol{x}',\boldsymbol{y}',\boldsymbol{z}')$, as illustrated by a hypothetical surface in Fig. 1, is defined by rotating $(\boldsymbol{x},\boldsymbol{y},\boldsymbol{z})$ by ϕ about $\boldsymbol{z}$, and then ψ about $\boldsymbol{y}$, such that y' is the outward unit normal direction of the solid surface. Where y' is calculated using the density gradient of the solid material particles within the surface cell, as shown in Eq. (18).

$$y' = -\nabla\rho_{\mathrm{s}}/|\nabla\rho_{\mathrm{s}}| \tag{18}$$

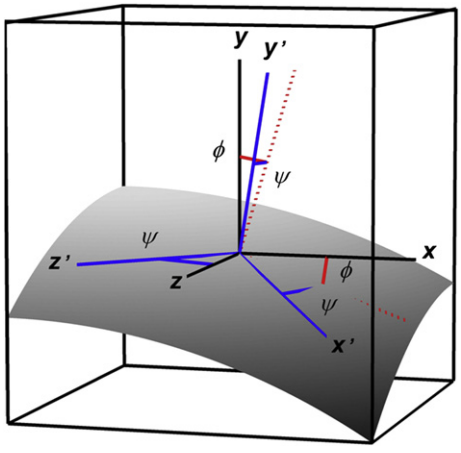

Fig. 1. Global and surface coordinate systems.

The material velocities in terms of $(\boldsymbol{x}', \boldsymbol{y}', \boldsymbol{z}')$ are obtained by applying the rotation matrix Q, given in Eq. (19), to $\boldsymbol{u}$ as shown in Eq. (20). By definition, Q is a real, orthogonal, special matrix ($Q^T = Q^{-1}$, $\det(Q) = 1$), in which the rows represent the $(\boldsymbol{x}', \boldsymbol{y}', \boldsymbol{z}')$ unit vectors as defined in the original $(\boldsymbol{x}, \boldsymbol{y}, \boldsymbol{z})$ system. Once the velocities are defined in terms of the $(\boldsymbol{x}', \boldsymbol{y}', \boldsymbol{z}')$ coordinates, the momentum exchange between materials is calculated for each surface coordinate direction, utilizing the numerical implementation of Eq. (6), with K_{rs}^{slip} in the $\boldsymbol{x}'$ and $\boldsymbol{z}'$ directions, and the no-slip H_{rs}^{slip} in the $\boldsymbol{y}'$ direction. Following the exchange of momentum between materials in the $(\boldsymbol{x}', \boldsymbol{y}', \boldsymbol{z}')$ system, the material velocities are then returned to the $(\boldsymbol{x}, \boldsymbol{y}, \boldsymbol{z})$ description utilizing Q^T as shown in Eq. (21). Numerically, if $y'_y = \pm 1 \pm 0.001$ then the surface normal is assumed to be already aligned with the global coordinate system and consequently no rotation is required; Q is then set equal to the identity matrix, rather than divide by zero as indicated in Eq. (19).

$$Q = \begin{bmatrix} x'_x & x'_y & x'_z \\ y'_x & y'_y & y'_z \\ z'_x & z'_y & z'_z \end{bmatrix} = \begin{bmatrix} \cos\phi\cos\psi & -\sin\phi & \cos\phi\sin\psi \\ \sin\phi\cos\psi & \cos\phi & \sin\phi\sin\psi \\ -\sin\psi & 0 & \cos\psi \end{bmatrix}$$

$$\rightarrow \begin{bmatrix} \dfrac{y'_y y'_x}{\sqrt{1-y'^2_y}} & -\sqrt{1-y'^2_y} & \dfrac{y'_y y'_z}{\sqrt{1-y'^2_y}} \\ y'_x & y'_y & y'_z \\ \dfrac{-y'_z}{\sqrt{1-y'^2_y}} & 0 & \dfrac{y'_x}{\sqrt{1-y'^2_y}} \end{bmatrix} \tag{19}$$

$$\sum_{s=1}^{N} \boldsymbol{u}'^{-}_s = \sum_{s=1}^{N} Q\boldsymbol{u}^{-}_s \tag{20}$$

$$\sum_{s=1}^{N} \boldsymbol{u}^{+}_s = \sum_{s=1}^{N} Q^T\boldsymbol{u}'^{+}_s \tag{21}$$

As described previously, the models for momentum and thermal energy exchange between materials, and consequently the slip flow modifications made to these models, are implemented in the MPM-ICE algorithm to calculate both the momentum and thermal energy change during the Lagrangian phase of the timestep, as well as the fluid advection velocity during Eulerian phase of the timestep.

3. Numerical results

To verify the methodology and implementation of the modifications described for the slip flow momentum and energy exchange models, several basic configurations, as outlined previously, are numerically evaluated. For each configuration, the numerical results are substantiated with grid convergence and order-of-accuracy studies, as well as comparison to previously established data. The MPM-ICE algorithm, and therefore each of the following studies, is explicit with time. Consequently, the maximum stable timestep for each simulation is limited by either diffusion ($\Delta t \leq 0.5 \cdot \Delta x^2/\nu$, $\Delta t \leq 0.5 \cdot \Delta x^2/\alpha$) or the speed-of-sound ($\Delta t \leq cfl \cdot \Delta x/(|\boldsymbol{u}| + c)$) for each material [33]. The cfl utilized for all of the following studies is $\sim$0.1. (Although, the ability to implicitly evaluate pressure exists in ICE, this does not increase the maximum timestep based on the speed-of-sound within the explicit MPM algorithm, and consequently, has not been utilized.) To obtain slow transient and steady state data, this explicit timestep is very limiting, particularly for refined grid resolutions, and as a result, the relatively simple configurations evaluated, require significant computing resources, which are only feasible due to MPM-ICE's parallel computing infrastructure [34]. The first two studies, which are the evaluation of velocity and temperature profiles of a rarefied gas between parallel plates, utilized 1 CPU for approximately 0.07–24 h, depending on the grid resolution. The third study, rarefied flow around a two-dimensional cylinder, utilizes 32 CPUs for approximately 78–900 h, depending on the grid resolution. And, the final study, the three-dimensional, flexible cylinder, utilizes 128 CPUs for about 32–600 h, again, depending on the grid resolution. The MPM-ICE algorithm is nondimensional, and so to reduce some of the numerical round-off error incurred with the long computation times, each of the microscale problems are evaluated in terms of μm, μs, fg, and K. It should be noted that this is not 'scaling' the problem in an attempt to reduce the number of required timesteps. If the problem were scaled, all of the nondimensional variables that describe the physical process, such as *Re*, *Ma*, *Pr*, etc., must remain constant, and therefore the corresponding nondimensional timeframe required for the physical process to occur, such as the Fourier number, *Fo*, will also remain constant. Thus, unless the problem of interest is changed, i.e. changing *Re*, *Ma*, *Pr*, etc., scaling Δx may increase Δ*t*, but will also proportionally increase the total time required to reach a specified point in the physical process, such as steady state, and the total number of explicit timesteps will remain the same.

3.1. Pressure driven flow between parallel plates

A pressure driven, fully developed, steady state, Newtonian, rarefied ideal gas flow between parallel plates with constant properties and negligible inertial forces, as specified in Fig. 2(a), is modeled to verify the accuracy and implementation of the slip flow momentum exchange modifications in the MPM-ICE algorithm. The analytic velocity solution used to verify the numerical data, Eq. (22), is obtained by integrating the momentum equation, $\mu(\partial^2 u/\partial y^2) = dP/dx$, twice, and applying the slip velocity boundary condition at the wall, $u|_{y=0} = \beta_v \lambda(\partial u/\partial y)_{y=0}$, and symmetry at the midplane, $(\partial u/\partial y)_{y=h/2} = 0$, and then normalizing by the resulting mean velocity, u_m.

$$\frac{u(y/h)}{u_m} = \frac{6(y/h - y^2/h^2 + 2\beta_v Kn)}{1 + 12\beta_v Kn} \tag{22}$$

Eq (22), as well as the Boltzmann equation solution presented by [35] for comparable conditions (hard sphere molecules, diffuse reflection, uniform pressure gradient, negligible inertial forces), are compared to the numerical data at steady state in Fig. 2(b) nad (c) for the parameters specified. The criterion used to establish that the flow is steady state is $|\boldsymbol{u}^{n+1} - \boldsymbol{u}^n/\boldsymbol{u}^{n+1}| \leq 10^{-10}$ for each control volume, where n is the number of timesteps. The time required to reach steady state varies with the grid resolution and *Kn*, however the longest time required to reach steady state for the evaluations presented in Table 1 is 0.065 μs. Consequently, all data are presented at 0.1 μs when each evaluation has unquestionably reached steady state.

Grid convergence, order-of-accuracy, and conservation of momentum exchange data for this configuration, as well as the total number of timesteps required to reach $t = 0.1$ μs, are reported in Table 1. The data in Table 1 for no-slip flow, $Kn_m = 0$, are produced using the original algorithm, while the data reported for $Kn_m = 0.0564$ and 0.1128 are obtained using the algorithm with the slip flow momentum exchange model. The L_2 norm error in Table 1 refers to the difference between the normalized numerical and analytical velocity profiles. The order-of-accuracy [33], p, computed with the L_2 norm errors, indicate that both the original and modified algorithm converge with increasing grid resolution with an order-of-accuracy of approximately 1.0, as expected based on the second-order spatial discretization utilized in the algorithm. Although not explicitly stated previously, the momentum exchange model must

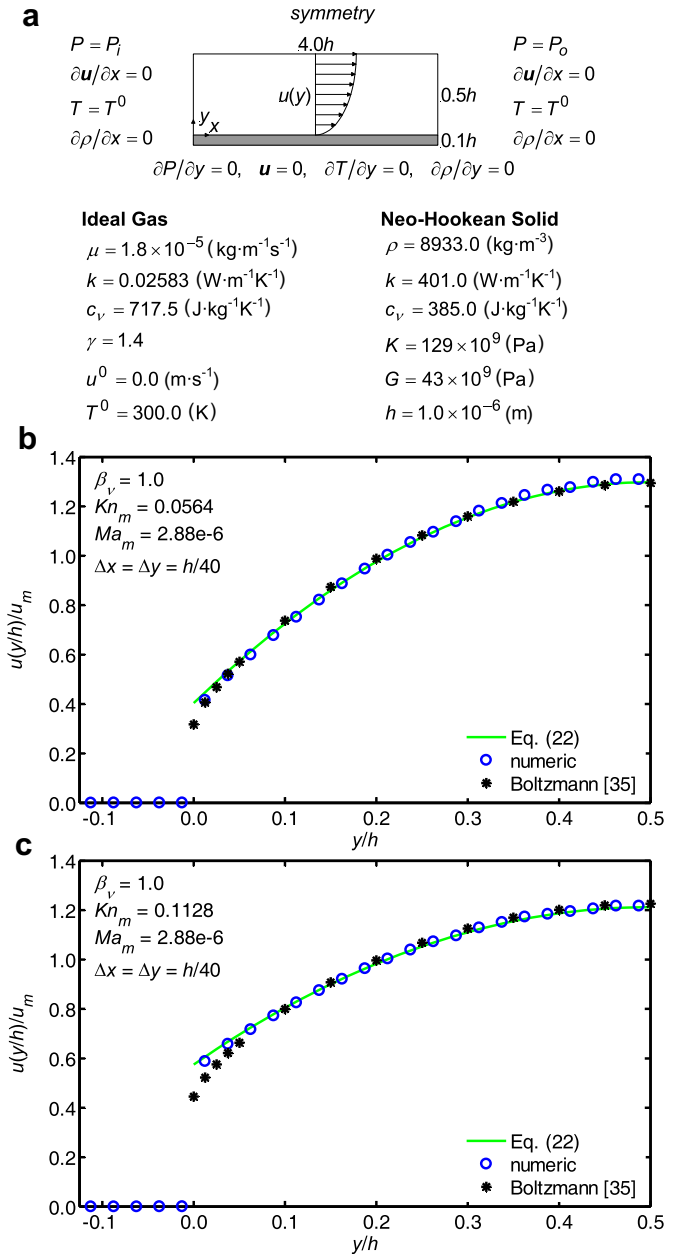

Fig. 2. Steady state ($t = 0.1$ μs) pressure driven flow between parallel plates: (a) problem specification, (b) Velocity profile, $Kn_m = 0.0564$, (c) Velocity profile, $Kn_m = 0.1128$.

Table 1
Grid resolution, order-of-accuracy, and conservation of momentum exchange for steady state ($t = 0.1$ μs) pressure driven flow between parallel plates.

Kn_m	Δy (=Δx)	L_2 $u(y/h)/u_m$	p	timesteps	RMS (exchange error/total)	
					x-momentum	y-momentum
0.0000	$h/10$	0.39	1.02	15,117	1.88×10^{-10}	1.61×10^{-1}
	$h/20$	0.22		60,403	7.45×10^{-12}	2.41×10^{-3}
	$h/40$	0.13		241,554	4.34×10^{-13}	4.76×10^{-4}
0.0564	$h/10$	0.15	0.96	15,117	2.26×10^{-10}	4.47×10^{-8}
	$h/20$	0.09		60,403	3.77×10^{-12}	1.70×10^{-6}
	$h/40$	0.05		241,553	1.13×10^{-13}	1.25×10^{-7}
0.1128	$h/10$	0.09	1.10	30,212	1.27×10^{-10}	2.37×10^{-7}
	$h/20$	0.05		120,787	2.98×10^{-12}	6.20×10^{-6}
	$h/40$	0.03		483,448	8.30×10^{-14}	1.20×10^{-6}

conserve momentum - meaning that, while, momentum is exchanged between materials, the net momentum of all the materials must be the same before and after the momentum exchange model is applied. The root-mean-square (*RMS*) x- and y- momentum exchange error reported in Table 1 is the *RMS* of the ratio of the net momentum exchange error to the net momentum for all timesteps. (The RMS y-momentum exchange error is larger than the RMS x-momentum exchange error because the net y-momentum is nearly zero.) The data in Fig. 2 and Table 1 indicate that the modified slip flow momentum exchange model accurately represents slip velocity boundary conditions compared to first-order boundary conditions, converges with the same order-of-accuracy as the original algorithm, and conserves the exchanged momentum.

3.2. Thermal conduction between parallel plates

The steady state thermal conduction of a stationary, constant property, rarefied ideal gas between two parallel plates of different temperatures, as specified in Fig. 3(a), is modeled with the MPM-ICE algorithm to verify the accuracy and implementation of the slip flow thermal energy exchange modifications. The analytic temperature profile used to verify the numerical data, Eq. (23), is derived by integrating the energy equation, $\partial^2 T/\partial y^2 = 0$, twice, and applying temperature jump boundary conditions at each wall, $T|_{y=0} = T_w - \Delta T + \beta_t \lambda (\partial T/\partial y)_{y=0}$ and $T|_{y=h} = T_w + \Delta T - \beta_t \lambda (\partial T/\partial y)_{y=h}$.

$$\frac{T(y/h) - T_w}{\Delta T} = \frac{-1 + 2(y/h)}{1 + 4\beta_t Kn} \tag{23}$$

Equation (23) is compared to the steady state numerical data in Fig. 3(b) for the parameters specified. The criterion used to establish that the flow is steady state is $|T^{n+1} - T^n/T^{n+1}| \leq 10^{-10}$ for each control volume. Again, the time required to reach steady state varies with the grid resolution and *Kn*, however the longest time required to reach steady state for the evaluations presented in Table 2 is 0.060 μs. Consequently, all data are presented 0.1 μs when each evaluation has unmistakably reached steady state.

Grid convergence, order-of-accuracy, and conservation of energy exchange data for this configuration, as well as the total number of timesteps required to reach $t = 0.1$ μs, are reported in Table 2. Once again, the data in Table 2 for continuum flow, $Kn_m = 0$, are produced using the original algorithm, while the data reported for $Kn_m = 0.0564$ and 0.1128 are obtained utilizing the slip flow energy exchange model. The L_2 norm error in Table 2 refers to the difference between the normalized numerical and analytical temperature profiles. The order-of-accuracy, computed with the L_2 norm errors, indicate that both the original and modified algorithm converge with increasing grid resolution with an order-of-accuracy of approximately 0.82. To ensure that the modified energy exchange model conserves energy, the *RMS* of the ratio of the net energy exchange error to the net energy for all timesteps is reported in Table 2. The data in Fig. 3 and Table 2 indicate that the modified slip flow energy exchange model accurately represents temperature jump when compared to first-order temperature jump boundary conditions, converges with the same order-of-accuracy as the original algorithm, and conserves the exchanged energy.

3.3. Low Reynolds number, infinite cylinder C_D and Nu

To verify that the MPM-ICE algorithm, with the slip flow momentum and energy exchange modifications, accurately represents a rarefied gas flow for a more complex geometry than those evaluated in *3.1* and *3.2*, flow around an infinite circular cylinder is evaluated. The flow behavior, drag coefficient, C_D, and Nusselt

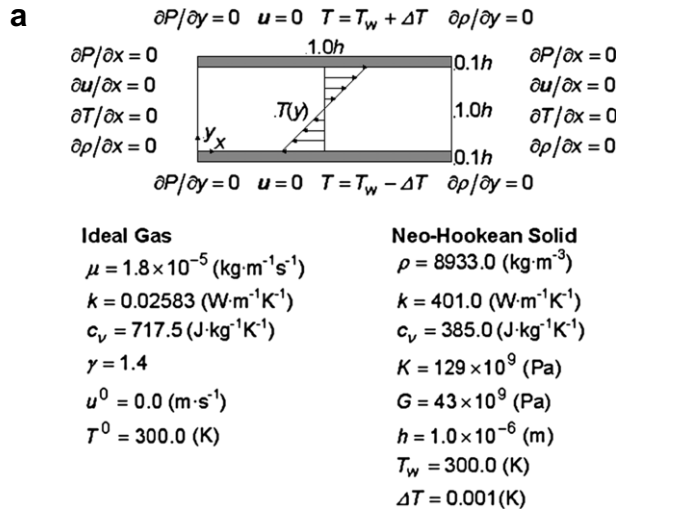

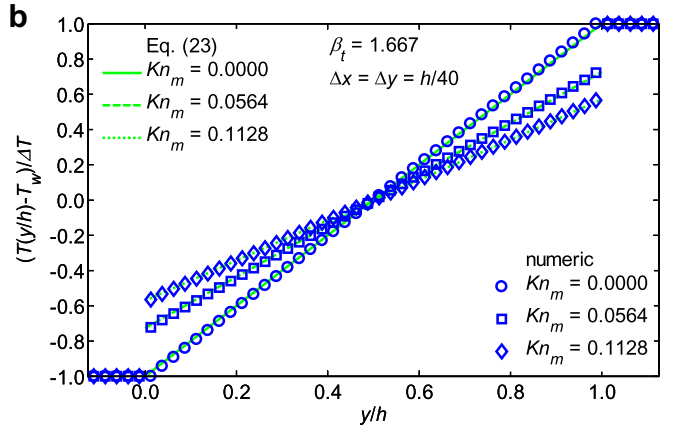

Fig. 3. Steady state (t = 0.1 μs) thermal conduction between parallel plates: (a) problem specification, (b) Temperature profiles, Kn_m = 0.0000, Kn_m = 0.0564, Kn_m = 0.1128.

number, *Nu*, for flow around an infinite cylinder are well known for continuum conditions. At very low Reynolds numbers, *Re* ≈ 0–5, viscous forces dominate and the flow is attached, steady, and symmetric. As *Re* increases, *Re* ≈ 5–47, the boundary layer separates and forms a pair of steady, symmetric, counter-rotating vortices in the cylinder wake. As *Re* increases further, the vortices grow and are alternately shed from either side of the cylinder, resulting in asymmetries and unsteady flow [36]. C_D and *Nu* are evaluated at very low *Re* in this study for several reasons. Most significantly, typical microfluidic system *Re* are very small, due to the small length scales. Additionally, the symmetry present at low *Re* may be utilized to reduce the computational problem size. Also, without flow separation, effects due to rarefaction only should be more evident. And, furthermore, some slip flow C_D and *Nu* data are available for comparison to numerical results at low *Re*, while none exists at higher *Re*. These data include an analytic C_D solution for creeping slip flow around a sphere [37], for which the rarefaction effects are expected to be comparable in magnitude to creeping slip flow around a cylinder; and, experimentally determined *Nu* for low *Re* slip flow around a cylinder [38].

Table 2
Grid resolution, order-of-accuracy, and conservation of energy exchange for steady state (t = 0.1 μs) thermal conduction between parallel plates.

Kn_m	Δy (=Δx)	L_2 $(T(y/h)-T_w)/\Delta T$	p	timesteps	RMS (exchange error/total) thermal energy
0.0000	h/10	0.18	0.79	20,148	8.02×10^{-13}
	h/20	0.11		80,531	2.02×10^{-12}
	h/40	0.07		322,064	3.91×10^{-12}
0.0564	h/10	0.09	0.82	15,117	2.87×10^{-13}
	h/20	0.06		60,403	7.52×10^{-13}
	h/40	0.04		241,553	1.30×10^{-12}
0.1128	h/10	0.05	0.84	30,212	5.88×10^{-13}
	h/20	0.03		120,786	1.55×10^{-12}
	h/40	0.02		483,088	2.47×10^{-12}

The numerical problem specification and flow parameters utilized to model flow around an infinite cylinder are presented in Fig. 4(a) and Table 3. Six data points are examined; three at *Re* = 0.01, such that the results can be compared to the solution for creeping slip flow around a sphere [37]; and, three at *Re* of roughly

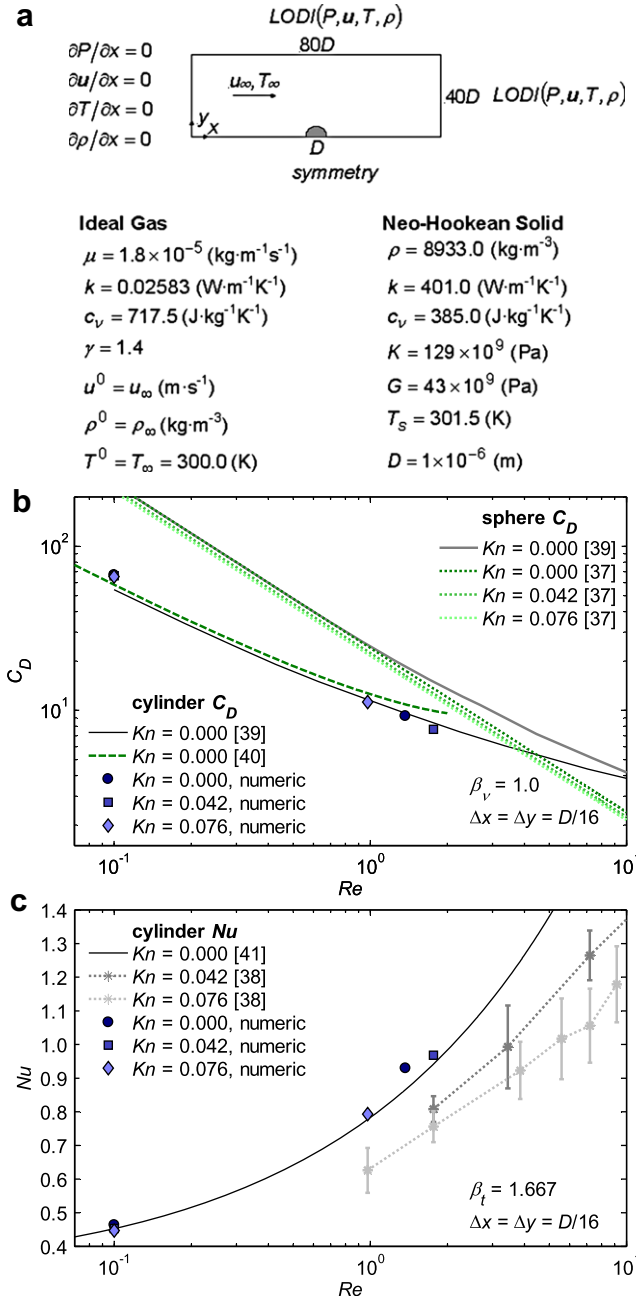

Fig. 4. Steady state (t = 180 μs) low Reynolds number, infinite cylinder C_D and *Nu*: (a) problem specification, (b) C_D, (c) *Nu*.

1.0, such that the results can be compared to the experimental results reported in [38], where the experimental *Nu* results were obtained at a constant *Ma* rather than a constant *Re*. To numerically approximate an unconfined cylinder at very low *Re* a large computational domain size and locally one-dimensional inviscid (LODI) boundary conditions, as described in [42], as indicated in Fig. 4(a), are used. To reduce the size of the resulting computational problem a multilevel grid is used. The grid size reported in Fig. 4 and Table 3 is the grid size immediately surrounding the cylinder; from 2.5*D* to 5*D* away from the cylinder center, the grid size is double the specified value; and, from 5D away from the cylinder center to the edge of the computational domain, the grid size is quadruple the specified value. The numerical C_D per unit length are obtained utilizing the standard definition, $C_D = F_D/(1/2)\rho_\infty u_\infty^2 D$, where (1/2) F_D is first computed via an integral *x*-momentum analysis around the symmetric cylinder. Similarly, the numerical *Nu* are calculated with the usual definition, $Nu = \overline{q}_{cyl}^{''} D/k_r(T_s - T_\infty)$, where $\overline{q}_{cyl}^{''}(\pi D/2)$, one-half of the thermal energy exchange rate per unit length due to the cylinder, is first obtained via an integral thermal energy analysis around the symmetric cylinder. The resulting, steady state (based on the steady state criteria previously specified in sections 3.1 and 3.2, all data are presented at $t = 180$ μs) C_D and *Nu* for each of the three gird resolutions examined, are presented in Table 3, and the highest grid resolution C_D and *Nu* are also plotted and compared to reference values in Fig. 4(b) and (c), respectively. The calculated order-of-accuracy for these six data points varies between 0.08 and 2.26 for C_D and −0.13 and 1.13 for *Nu*, however the average grid resolution order-of-accuracy is ∼1.0 for C_D and ∼0.5 for *Nu*.

The numerically determined infinite cylinder C_D reported in Table 3 and Fig. 4(b), for continuum flow, $Kn = 0.0$, is within 4.0% of the reference value [39] at $Re = 1.37$ ($\Delta x = \Delta y = D/16$), and within ∼18% of the reference values [39,40] at $Re = 0.1$. The larger difference at $Re = 0.1$, is because the reference C_D values are for an unconfined cylinder, which cannot be accurately numerically simulated, particular at low *Re*, where viscous effects are dominant, but can only be approximated at the computational boundaries. The effect of rarefaction, quantified by *Kn*, on the numerically determined cylinder C_D is comparable to, although less than, the analytically predicted effect of *Kn* on sphere C_D. The sphere C_D is reduced 6.71% for $Kn = 0.042$, and 10.44% for $Kn = 0.076$, for $\beta_v = 1$ and all *Re* [37]. The numerically determined cylinder C_D is approximately 1–2% less for $Kn = 0.042$, and 2–3% less for $Kn = 0.076$. For the $Re \approx 1.0$ data, the reduction in C_D with *Kn* is calculated relative to the continuum flow data [39], since the C_D data are not calculated at exactly the same *Re*. The agreement between the numerical C_D data and the reference values at $Kn = 0.0$, and the reduction in C_D due to rarefaction, indicate that the algorithm is able to model a rarefied flow around an infinite circular cylinder.

The numerically determined infinite cylinder *Nu* data reported in Table 3 and Fig. 4(c) are in reasonable agreement with both the continuum correlation [41] and the experimental slip flow data [38]. For the highest grid resolution, the numerical *Nu* for continuum flow, $Kn = 0.0$, are on average within 5% of the correlation values. The effect of rarefaction on the numerically determined *Nu* at $Re \sim 0.1$, is roughly a 4% decrease at $Kn = 0.042$, and a 6% decrease at $Kn = 0.076$, which is somewhat less than expected based on the experimental values, in which there is a 14% decrease at $Kn = 0.042$, and a 19% decrease at $Kn = 0.076$. The numerical slip flow *Nu* at $Re \approx 1$ are likely higher than the experimental slip flow *Nu*, due, in part, to the approximation of the numerical thermal accommodation coefficient, $\sigma_t = 1$. Experimentally measured σ_t are often near unity, but may be any value between zero and one. A value of σ_t less than one will result in an increase in the temperature jump at the surface, which will then produce a decrease in *Nu*. Overall, the agreement between the numerical *Nu* data, the correlation data [41] and the experimental data [38], indicates that the MPM-ICE algorithm, with the slip flow momentum and energy exchange modifications, successfully represents the thermal/hydrodynamic flow behavior of a rarefied gas around an infinite circular cylinder. Future studies, with a broader range of *Kn* and *Re* values, may be useful to further verify the results presented in this study.

3.4. Unsteady slip flow fluid-structure-interaction

To verify that the algorithm is capable of accurately predicting unsteady fluid-structure-interaction with a rarefied flow, the thermal/structural response of a damped-oscillatory three-dimensional cylindrical fin, subject to uniform, rarefied flow, as illustrated in Fig. 5(a), is evaluated. This particular configuration is evaluated because there are several similar microscale applications, including, atomic force microscope measurements [7,9,18], heat exchangers [5], and biosensors and actuators [13,14,17]. In this evaluation, the fin initially has zero displacement, $\delta(y,0) = 0$, zero velocity, $\partial\delta(y,0)/\partial t = 0$, and a uniform temperature equal to the constant fin base temperature, $T(y,0) = T(0,t) = T_b$. The rarefied gas initially has a uniform velocity, u_∞, and a uniform temperature, T_∞, which is less than the fin base temperature. As the system is set in motion, the sudden fluid force on the fin results in its displacement and subsequent damped oscillation while it simultaneously transfers heat to the fluid.

Table 3
Grid resolution, order-of-accuracy, and comparison to reference values for steady state ($t = 180$ μs) low Reynolds number, infinite cylinder C_D and *Nu*.

Kn	*Re*	Δ*y* (=Δ*x*)	C_D	*p*	C_D [39] (*Kn* = 0)	C_D [40] (*Kn* = 0)	*Nu*	*p*	*Nu* [41] (*Kn* = 0)	*Nu* [38]
0.000	0.10	D/4	76.43	0.84	54.42	58.39	0.493	0.63	0.453	–
		D/8	70.35				0.475			
		D/16	66.95				0.464			
0.042	0.10	D/4	71.98	2.26	54.42	58.39	0.470	1.13	0.453	–
		D/8	67.14				0.458			
		D/16	66.14				0.453			
0.076	0.10	D/4	70.62	0.08	54.42	58.39	0.458	−0.13	0.453	–
		D/8	67.90				0.453			
		D/16	65.32				0.447			
0.000	1.37	D/4	10.68	0.88	9.62	10.87	1.012	0.34	0.866	–
		D/8	9.75				0.966			
		D/16	9.25				0.930			
0.042	1.77	D/4	8.71	0.87	8.41	9.93	1.045	0.35	0.942	0.81 ± 0.04
		D/8	8.04				1.002			
		D/16	7.67				0.968			
0.076	0.98	D/4	12.52	0.85	11.63	12.71	0.841	0.49	0.777	0.63 ± 0.07
		D/8	11.70				0.813			
		D/16	11.24				0.793			

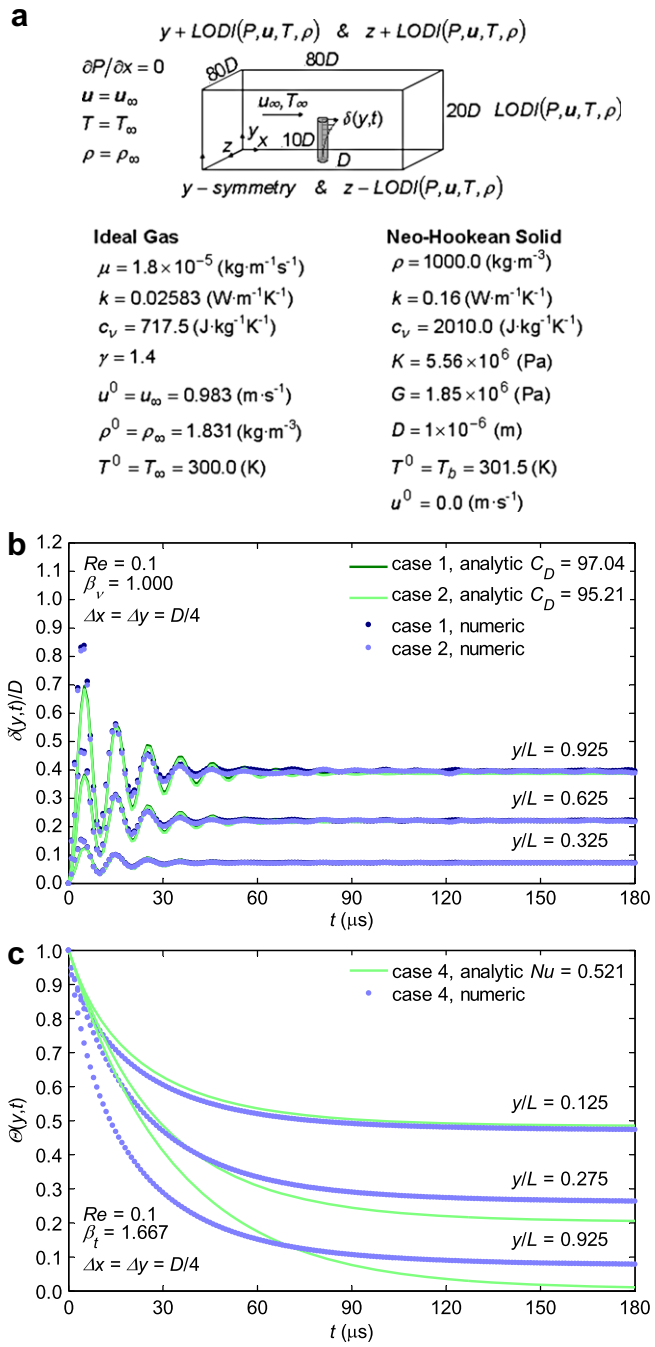

Fig. 5. Unsteady slip flow fluid-structure-interaction: (a) problem specification, (b) $\delta(y,t)/D$, (c) $\Theta(y,t)$.

To verify the numerical simulation of this system, comparisons to analytic solutions are necessary. The governing equation for beam vibration, the Euler–Bernoulli equation [43], may be solved with the force of the fluid modeled as a Stokes drag force, $F_D(y,t)/L = C\mu(u_\infty - \partial\delta(y,t)/\partial t)$, which is accurate for very low Re flow. The Stokes drag coefficient, C, is related to the typical drag coefficient as $C_D = 2C/Re$. The Euler–Bernoulli equation, boundary conditions, initial conditions, and resulting analytic fin displacement solution, $\delta(y,t)$, as obtain by the standard solution methods of separation-of-variables and orthogonality, are summarized in Table 4. The governing energy equation for the fin, boundary conditions (with a convective tip condition), initial conditions, and resulting analytic transient temperature distribution, obtained by the standard solution methods of separation-of-variables and orthogonality, are summarized in Table 5. To derive the unsteady, normalized, analytic temperature distribution, $\Theta(y,t)$, it is assumed that the transient fin temperature varies only axially and that the convective heat transfer coefficient, h, is uniform and constant. In reality, however, h varies both spatially and temporally, and the fin cross sectional temperature will also vary slightly ($Bi_D \approx 0.1$). Consequently, the analytic $\Theta(y,t)$ solution presented in Table 5, is only expected to provide an approximate comparison to the numerical data.

The problem specification and flow parameters utilized to model the transient fin displacement and temperature are given in Fig. 5(a) and Table 6. As specified in Table 6, both continuum flow, $Kn = 0$, and rarefied flow, $Kn = 0.042$, are evaluated for both a flexible ($E = 5 \times 10^6$ Pa) and a rigid fin. The transient numerical solution is obtained for $0 \le t \le 180$ μs, with data recorded every 1.0 μs. For each timestep recorded, the fin cross sectional average of the material particle displacement and temperature are obtained at 20 equally spaced axial intervals (for all grid resolutions evaluated).

The normalized numerical fin displacements, $\delta(y,t)/D$, for the flexible cases at the highest grid resolution ($\Delta x = \Delta y = D/4$), are presented and compared to the analytic solution in Fig. 5(b), at several axial locations, $y/L = 0.325$, 0.625, and 0.925. All of the parameters required to calculate the analytic fin displacement (Table 4), are specified in Fig. 5(a), except the Stokes drag coefficient, $C = ReC_D/2$, which is unknown. Therefore, for cases 1 and 2, which are the flexible fins, the C_D that results in the smallest L_2 norm error between the analytic and numeric $\delta(y,t)/D$ data is utilized to obtain the analytic solution. The resulting C_D values and L_2 norm errors, for cases 1 and 2, are reported in Table 6, for each grid resolution evaluated. Because C_D is calculated from the fin deflection, no C_D or L_2 norm error is reported for the rigid cases, 3 and 4. The expected C_D for an unconfined, infinite cylinder, at $Re = 0.1$ is 58.39 [40]. The numerical finite, cylindrical fin C_D reported in Table 6 for cases 1 and 2, are larger than 58.39, due to the course grid resolution utilized, the effects of flow around the tip of the fin [36], and the proximity of the computational boundaries to the fin, as discussed previously in 3.3. C_D for $Kn = 0.042$ are approximately 1–2% less than C_D for $Kn = 0.0$. Correspondingly, the amplitude of the fin's displacement is slightly lower for $Kn = 0.042$, compared to $Kn = 0.0$, and the time required to reach steady state is slightly longer for $Kn = 0.042$ compared to $Kn = 0.0$. Although this reduction in C_D due to rarefaction is slight, it is consistent in magnitude with the reduction in C_D due to rarefaction for the infinite cylinder, as presented previously in Fig. 4(b).

All of the parameters required to calculate the analytic transient temperature distribution (Table 5), are specified in Fig. 5(a), except the heat transfer coefficient, $h = Nuk_f/D$, which is unknown. Consequently, the Nu that results in the minimum L_2 norm error between the analytic and numeric normalized temperature distribution, $\Theta(y,t)$, is utilized to obtain the analytic solution. The resulting Nu and L_2 norm errors for each case and grid resolution are reported in Table 6. The numeric and analytic $\Theta(y,t)$, for case 4 are compared at several axial locations, $y/L = 0.125$, 0.275, 0.925, in Fig. 5(c), for the higher grid resolution ($\Delta x = \Delta y = D/4$). Only data for case 4 are presented in Fig. 5(c), since the data for each of the other three cases are very similar. As expected, the numeric and analytic $\Theta(y,t)$ in Fig. 5(c) are comparable, but not identical, since h in the simulation is not uniform or constant, as assumed in the analytic solution. For the four cases considered, rarefaction effects decrease Nu by ~1–2%, and the effect of the flexible fin's motion increases Nu by ~2%. The expected steady state Nu for an unconfined, infinite cylinder, at $Re = 0.1$ is 0.453 [41]. Although, the transient numerical Nu data are obtained with a very course grid resolution, and the fin is finite in length and confined by computational boundaries, the Nu reported in Table 6, are still comparable

Table 4
Analytic solution for transient fin displacement.

Governing equation

$\partial^2\delta(y,t)/\partial t^2 + (C\mu/\rho_s A_c)\partial\delta(y,t)/\partial t + (EI/\rho_s A_c)\partial^4\delta(y,t)/\partial y^4 = C\mu u_\infty/\rho_s A_c$

Boundary Conditions

$\delta(0,t) = 0$
$\partial\delta(0,t)/\partial y = 0$
$\partial^2\delta(L,t)/\partial y^2 = 0$
$\partial^3\delta(L,t)/\partial y^3 = 0$

Initial Conditions

$\delta(y,0) = 0$
$\partial\delta(y,0)/\partial t = 0$

Solution

$\delta(y,t) = \delta_p(y) + \sum_{n=1}^{\infty} Y_n(y)A_n\exp(-\varsigma_n\omega_n t)[\cos(\omega_{d,n}t) + (\varsigma_n\omega_n/\omega_{d,n})\sin(\omega_{d,n}t)]$

$\delta_p(y) = (C\mu u_\infty y^2/24EI)(6L^2 - 4Ly + y^2)$

$Y_n(y) = \cosh(\beta_n y) - \cos(\beta_n y) - \sigma_n\sinh(\beta_n y) + \sigma_n\sin(\beta_n y)$
$\sigma_n = [\sinh(\beta_n L) - \sin(\beta_n L)]/[\cosh(\beta_n L) + \cos(\beta_n L)]$
$\cosh(\beta_n L)\cos(\beta_n L) = -1$
$A_n = -\int_0^L \delta_p(y)Y_n(y)dy / \int_0^L Y_n^2(y)dy$
$\omega_n = \beta_n^2\sqrt{EI/\rho_s A_c}$
$\varsigma_n = (C\mu/2\rho_s A_c\beta_n^2)\sqrt{\rho_s A_c/EI}$
$\omega_{d,n} = \omega_n\sqrt{1-\varsigma_n^2}$

n	$\beta_n L$	$A_n/(C\mu u_\infty L^4/24EI)$
1	1.8751	-1.5201×10^{0}
2	4.6941	-2.1450×10^{-2}
3	7.8548	-1.6041×10^{-3}
4	10.9955	-2.9866×10^{-4}
5	14.1372	-8.5002×10^{-5}

Table 5
Analytic solution for transient fin temperature distribution.

Governing equation

$\partial^2 T(y,t)/\partial y^2 - m^2[T(y,t) - T_\infty] = (\rho_s c_{v,s}/k_s)\partial T(y,t)/\partial t$
$m^2 = 4h/Dk_s$

Boundary Conditions

$T(0,t) = T_b$
$T(L,t) - T_\infty = -(k/h)\partial T(L,t)/\partial y|_{y=L}$

Initial Conditions

$T(y,0) = T_b$

Solution

$(T(y,t) - T_\infty)/(T_b - T_\infty) = \Theta(y,t) = \Theta_p(y) + \sum_{n=1}^{\infty} C_n\exp[-(k_s t/\rho_s c_{v,s})(m^2 + \Lambda_n^2)]\sin(\Lambda_n y)]$
$\Theta_p(y) = (\cosh[m(L-y)] + (h/mk_s)\sinh[m(L-y)])/(\cosh(mL) + (h/mk_s)\sinh(mL))$
$\tan(\Lambda_n L) = -(k_s/hL)(\Lambda_n L)$
$C_n = \left(\frac{4\Lambda_n}{2\Lambda_n L - \sin(2\Lambda_n L)}\right)\left\{\frac{1-\cos(\Lambda_n L)}{\Lambda_n} - \frac{\Lambda_n - [\Lambda_n\cos(\Lambda_n L) + (h/k_s)\sin(\Lambda_n L)]/[\cosh(mL) + (h/mk_s)\sinh(mL)]}{m^2 + \Lambda_n^2}\right\}$

in magnitude. The data presented in Fig. 5 and Table 6 indicate that the MPM-ICE algorithm, with the slip flow momentum and energy exchange modifications, converges with approximately first-order numerical accuracy. And, that the algorithm is capable of qualitatively predicting the unsteady fluid-structure-interaction of a damped-oscillatory three-dimensional cylindrical fin, subject to an impulsively started uniform, rarefied flow, as compared to the analytically predicted displacement and temperature solutions.

Table 6
Problem specification, error evaluation, and C_D and Nu results for the transient, flexible fin displacement and temperature response.

Case	Kn	Re	E (Pa)	Δy ($=\Delta x$)	C_D	L_2 $\delta(y,t)/D$	Nu	L_2 $\Theta(y,t)$
1	0.000	0.10	5.0×10^6	D/1	129.31	2.11	0.616	4.37
				D/2	105.26	1.37	0.535	4.29
				D/4	97.04	1.10	0.526	3.63
2	0.042	0.10	5.0×10^6	D/1	130.99	2.02	0.564	4.91
				D/2	101.90	1.40	0.538	4.10
				D/4	95.21	1.10	0.525	3.47
3	0.000	0.10	rigid	D/1	–	–	0.561	5.00
				D/2	–	–	0.534	4.23
				D/4	–	–	0.525	3.59
4	0.042	0.10	rigid	D/1	–	–	0.561	4.97
				D/2	–	–	0.534	3.92
				D/4	–	–	0.521	3.31

4. Summary

This study modifies the momentum and thermal energy exchange models of an existing, continuum based, multifield, compressible, unsteady, Eulerian-Lagrangian FSI algorithm, such that, for a rarefied gas in the slip flow regime, the equivalent of first-order slip velocity and temperature jump boundary conditions are achieved at fluid-solid surfaces, which may move and deform with time. The momentum and thermal energy exchange models are modified by utilizing slip flow momentum and energy exchange coefficients that are derived as a function of the level of rarefaction from the original first-order slip velocity and temperature jump boundary conditions. The momentum and energy exchange models with the slip flow momentum and energy exchange coefficients are then applied at fluid-solid surfaces such that momentum is exchanged between the rarefied gas and the solid material in the fluid-solid surface normal and tangential coordinate directions, rather than arbitrary global coordinates, and slip flow in the surface tangential direction is realized.

Following the development and implementation of the slip flow momentum and energy exchange modifications, several basic

configurations are considered to verify the resulting algorithm's capabilities. The configurations include the velocity profiles of a rarefied gas between parallel plates, temperature profiles of a rarefied gas between parallel plates, drag coefficients, C_D, and Nusselt numbers, Nu, for low Reynolds number rarefied flow around an infinite cylinder, and the transient, thermal/structural response of a damped-oscillatory three-dimensional finite cylinder subject to an impulsively started uniform, rarefied flow. For each configuration, the numerical results are evaluated with grid convergence and order-of-accuracy studies, as well as comparison to reference data. Results of these evaluations indicate 1) that the slip flow momentum and energy exchange models conserve exchanged momentum and energy, respectively, and 2) that with these models, the algorithm is capable of modeling steady and unsteady fluid-structure-interaction with rarefaction effects with accuracy approximately equivalent to the first-order slip velocity and temperature jump boundary conditions. There are many microscale systems for which both rarefaction and fluid-structure-interaction effects are significant. Based on the modifications and verifications presented in this study, it is expected that the MPM-ICE algorithm, with the slip flow momentum and energy exchange modifications, has the unique ability to accurately model and evaluate these systems.

References

[1] J.C. Maxwell, On stresses in rarefied gases arising from inequalities of temperature, Phil. Trans. R. Soc. Lond 170 (1879) 231–256.
[2] M. Smoluchowski, Ueber wärmeleitung in verdünnten gasen, Annal. Phys. Chem. 64 (1898) 101–130.
[3] G.M. Whitesides, A.D. Stroock, Flexible methods for microfluidics, Phys. Today 54 (6) (2001) 42–48.
[4] M.J. Madou, Fundamentals of Microfabrication: The Science of Miniaturization, second ed.. CRC Press LLC, Boca Raton, Florida, 2002.
[5] J.S. Go, Design of a microfin array heat sink using flow-induced vibration to enhance the heat transfer in the laminar flow regime, Sensor. Actuator. Phys. 105 (2) (2003) 201–210.
[6] A. Alexeev, R. Verberg, A.C. Balazs, Motion of compliant capsules on corrugated surfaces: a means of sorting by mechanical properties, J. Polym. Sci. B Polym. Phys. 44 (18) (2006) 2667–2678.
[7] S. Basak, A. Raman, S.V. Garimella, Hydrodynamic loading of microcantilevers vibrating in viscous fluids, J. Appl. Phys. 99 (11) (2006) 114906.
[8] Y. Bozhi, L. Qiao, A planar compliance-based self-adaptive microfluid variable resistor, IEEE ASME J. Microelectromech. Syst. 16 (2) (2007) 411–419.
[9] D.G. Cole, R.L. Clark, Fluid-structure interaction in atomic force microscope cantilever dynamics and thermal response, J. Appl. Phys. 101 (3) (2007) 034303.
[10] S. Desai, M. Lovell, J. Cordle, Coupled field analysis of a piezoelectric bimorph disc in a direct write process, Compos. B Eng. 38 (7–8) (2007) 824–832.
[11] O. Ducloux, A. Talbi, L. Gimeno, R. Viard, P. Pernod, V. Preobrazhensky, A. Merlen, Self-oscillation mode due to fluid-structure interaction in a micromechanical valve, Appl. Phys. Lett. 91 (3) (2007) 034101.
[12] J. Jeong, C.N. Kim, A numerical simulation on diffuser-nozzle based piezoelectric micropumps with two different numerical models, Int. J. Numer. Meth. Fluid 53 (4) (2007) 561–571.
[13] P. Jungyul, R. Suk-Kyu, K. Jinseok, C. Junghun, B. Jeongeun, P. Sukho, K. Byungkyu, L. Sang Ho, A three-dimensional model of fluid-structural interactions for quantifying the contractile force for cardiomyocytes on hybrid biopolymer microcantilever, J. Biomech. 40 (13) (2007) 2823–2830.
[14] V.V. Khatavkar, P.D. Anderson, J.M.J. den Toonder, H.E.H. Meijer, Active micromixer based on artificial cilia, Phys. Fluid 19 (8) (2007) 083605.
[15] G. Krishnan, J.W. Daily, J. Nabity, Simulation of an electrostatically driven microinjector, J. Propul. Power 23 (6) (2007) 1321–1326.
[16] K.L. Kudar, P.W. Carpenter, Numerical investigation and feasibility study of a PZT-driven micro-valve pulsed-jet actuator, Flow Turbul. Combust. 78 (3–4) (2007) 223–254.
[17] K.-M. Lim, H. Li, A coupled boundary element/finite difference method for fluid-structure interaction with application to dynamic analysis of outer hair cells, Comput. Struct. 85 (11–14) (2007) 911–922.
[18] V. Ostasevicius, R. Dauksevicius, R. Gaidys, A. Palevicius, Numerical analysis of fluid-structure interaction effects on vibrations of cantilever microstructure, J. Sound Vib 308 (3–5) (2007) 660–673.
[19] G.-Y. Zhou, S.-T. Tu, Viscoelastic analysis of rectangular passage of microchanneled plates subjected to internal pressure, Int. J. Solid Struct. 44 (21) (2007) 6791–6804.
[20] A.K. Pandey, R. Pratap, F.S. Chau, Effect of pressure on fluid damping in MEMS torsional resonators with flow ranging from continuum to molecular regime, Exp. Mech. 48 (1) (2008) 91–106.
[21] F. Harlow, A. Amsden, Numerical calculation of almost incompressible flow, J. Comput. Phys. 3 (1968) 80–93.
[22] B.A. Kashiwa, N.T. Padial, R.M. Rauenzahn, W.B. VanderHeyden, A cell-centered ICE method for multiphase flow simulations, Los Alamos National Laboratory Technical Report LA-UR-93-3922, 1993.
[23] J.U. Brackbill, D.B. Kothe, H.M. Ruppel, FLIP: a low-dissipation, particle-in-cell method for fluid flow, Comput. Phys. Comm. 48 (1) (1987) 25–38.
[24] D. Sulsky, Z. Shi-Jian, H.L. Schreyer, Application of a particle-in-cell method to solid mechanics, Comput. Phys. Comm. 87 (1–2) (1995) 236–252.
[25] B.A. Kashiwa, A multifield model and method for fluid-structure interaction dynamics, Los Alamos National Laboratory Technical Report LA-UR-01-1136, 2001.
[26] J.E. Guilkey, T. Harman, A. Xia, B. Kashiwa, P. McMurtry, An Eulerian-Lagrangian approach for large deformation fluid structure interaction problems, part 1: algorithm development, in: S.K. Chakrabarti (Ed.), Fluid Structure Interaction II: Proceedings of the Second International Conference on Fluid Structure Interaction, Cadiz, Spain, WIT Press, Boston, 2003, pp. 143–156.
[27] T. Harman, J.E. Guilkey, B. Kashiwa, J. Schmidt, P. McMurtry, An Eulerian-Lagrangian approach for large deformation fluid structure interaction problems, part 2: Multi-physics simulations within a modern computational framework, in: S.K. Chakrabarti (Ed.), Fluid Structure Interaction II: Proceedings of the Second International Conference on Fluid Structure Interaction, Cadiz, Spain, WIT Press, Boston, 2003, pp. 157–166.
[28] J.E. Guilkey, T.B. Harman, B. Banerjee, An Eulerian–Lagrangian approach for simulating explosions of energetic devices, Comput. Struct. 85 (2007) 660–674.
[29] J. van Rij, T. Harman, T. Ameel, The effect of creep flow on two-dimensional isoflux microchannels, Int. J. Thermal Sci. 46 (11) (2007) 1095–1103.
[30] J. van Rij, T. Ameel, T. Harman, The effect of viscous dissipation and rarefaction on rectangular microchannel convective heat transfer, Int. J. Thermal Sci. 48 (2) (2009) 271–281.
[31] J. van Rij, T. Ameel, T. Harman, An evaluation of secondary effects on microchannel frictional and convective heat transfer characteristics, Int. J. Heat Mass Transfer 52 (11–12) (2009) 2792–2801.
[32] C. Xiong, Use of simplified chemical kinetics in the simulation of combustion and explosions, PhD thesis, The University of Utah, Salt Lake City, UT, 2007.
[33] J.H. Ferziger, M. Peri&cacute, Computational Methods for Fluid Dynamics, second ed. Springer, New York, 1999.
[34] S.G. Parker, J. Guilkey, T. Harman, A component-based parallel infrastructure for the simulation of fluid-structure interaction, Eng. Comput. 22 (3–4) (2006) 277–292.
[35] T. Ohwada, Y. Sone, K. Aoki, Numerical analysis of the Poiseuille and thermal transpiration flows between two parallel plates on the basis of the Boltzmann equation for hard-sphere molecules, Phys. Fluids 1 (12) (1989) 2042–2049.
[36] G.J. Sheard, K. Hourigan, M.C. Thompson, Computations of the drag coefficients for low-Reynolds-number flow past rings, J. Fluid Mech. 526 (2005) 257–275.
[37] R.W. Barber, Y. Sun, X.J. Gu, D.R. Emerson, Isothermal slip flow over curved surfaces, Vacuum 76 (1) (2004) 73–81.
[38] L.V. Baldwin, Slip-flow heat transfer from cylinders in subsonic airstreams, Lewis Flight Propulsion Laboratory, National Advisory Committee for Aeronautics Technical Note NACA-TN-4369, 1958.
[39] H. Schlichting, K. Gersten, Boundary-layer Theory, eight ed. Springer, New York, 2000.
[40] Sir H. Lamb, Hydrodynamics, University Press, Cambridge, 1932.
[41] S.W. Churchill, M. Bernstein, Correlating equation for forced convection from gases and liquid to a circular cylinder in crossflow, J. Heat Tran 99 (2) (1977) 300–306.
[42] J.C. Sutherland, C.A. Kennedy, Improved boundary conditions for viscous, reacting, compressible flows, J. Comput. Phys. 191 (2003) 502–524.
[43] D.J. Inman, Engineering Vibration, Prentice Hall, Englewood Cliffs, N.J, 1994.